JACS
JOURNAL OF THE AMERICAN CHEMICAL SOCIETY



Article

# Rational Design of Covalent Cobaloxime-COF Hybrids for Enhanced Photocatalytic Hydrogen Evolution

Kerstin Gottschling, Gökcen Savasci, Hugo A. Vignolo-González, Sandra Schmidt, Philipp Mauker, Tanmay Banerjee, Petra Rovó, Christian Ochsenfeld, and Bettina V. Lotsch

*J. Am. Chem. Soc.*, **Just Accepted Manuscript** • DOI: 10.1021/jacs.0c02155 • Publication Date (Web): 20 Jun 2020

# Rational Design of Covalent Cobaloxime-COF Hybrids for Enhanced Photocatalytic Hydrogen Evolution

Kerstin Gottschling,[†,‡,¶,§] Gökcen Savasci,[†,‡,¶,§] Hugo Vignolo-González,[†] Sandra Schmidt,[‡] Philipp Mauker,[‡,§] Tanmay Banerjee,[†] Petra Rovó,[‡,§] Christian Ochsenfeld,[‡,†,¶,§] and Bettina V. Lotsch*[,†,‡,¶,§]

†*Max Planck Institute for Solid State Research, Heisenbergstr. 1, 70569 Stuttgart, Germany*
‡*Department of Chemistry, University of Munich (LMU), Butenandtstr. 5-13, 81377 Munich, Germany*
¶*Cluster of Excellence e-conversion, Lichtenbergstrasse 4a, 85748 Garching, Germany*
§*Center for Nanoscience (CeNS), Schellingstr. 4, 80799 Munich, Germany*
Received June 19, 2020; E-mail: b.lotsch@fkf.mpg.de

**Abstract:**

Covalent organic frameworks (COFs) display a unique combination of chemical tunability, structural diversity, high porosity, nanoscale regularity, and thermal stability. Recent efforts are directed at using such frameworks as tunable scaffolds for chemical reactions. In particular, COFs have emerged as viable platforms for mimicking natural photosynthesis. However, there is an indisputable need for efficient, stable, and economical alternatives for the traditional platinum-based co-catalysts for light-driven hydrogen evolution. Here, we present azide-functionalized chloro(pyridine)cobaloxime hydrogen-evolution co-catalysts immobilized on a hydrazone-based COF-42 backbone which shows improved and prolonged photocatalytic activity with respect to equivalent physisorbed systems. Advanced solid-state NMR and quantum chemical methods allow us to elucidate details of the improved photoreactivity and the structural composition of the involved active site. We found that a genuine interaction between the COF backbone and the cobaloxime facilitates re-coordination of the co-catalyst during the photoreaction, thereby improving the reactivity and hindering degradation of the catalyst. The excellent stability and prolonged reactivity make the herein reported cobaloxime-tethered COF materials promising hydrogen evolution catalysts for future solar fuel technologies.

## Introduction

Identifying competitive alternatives to fossil-fuel-based energy constitutes one of the main research goals of this decade. Nature-inspired processes, like artificial photosynthesis, guide the way to a green and sustainable solution.[1–3] Covalent organic frameworks (COFs) have been emerging as new materials in this context.[4,5] COFs consist of light-elements only and their bottom-up synthesis enables high versatility and tunability on a molecular level while benefiting from high stability and crystallinity due to covalent bonding in plane and *via* $\pi$-$\pi$ stacking out of plane.[6–9] Most reports of COFs as photosensitizers for light-driven hydrogen evolution use platinum as a co-catalyst;[10–12] hydrogen evolution rates up to 16.3 mmol $h^{-1}$ $g^{-1}$ have been reported in this context.[13] Recent studies showed that the precious metal platinum can be replaced by earth-abundant molecular co-catalysts, namely chloro(pyridine)cobaloxime and related complexes.[14–16] These co-catalysts are well-known and well-defined while offering high tunability, which facilitate their incorporation into photoactive organic and inorganic systems.[17–19] Cobaloximes feature low overpotential for the hydrogen evolution reaction and have been used in heterogeneous systems with MOFs[20,21] and carbon nitrides,[22,23] as well as physisorbed to COFs.[14] A major drawback of molecular proton reduction catalysts physisorbed to photosensitizers is their photodeactivation over time[24–26] and rate limitations due to diffusion-controlled mechanisms. While previous attempts[14] used molecular cobaloxime catalysts in solution, in this work we report photocatalytic hydrogen evolution with molecular cobaloxime catalysts covalently tethered to the COF backbone, yielding unprecedented insights into the nature of the active site and the COF-co-catalyst interface. By comparison with equivalent unbound, i.e. physisorbed systems we show how the modification of the hydrazone-based COF-42 and attachment of functionalized chloro(pyridine)cobaloxime lead to more efficient hydrogen evolution in a water/acetonitrile mixture under visible light illumination in the presence of a sacrificial electron donor. The structural composition of the photoreaction is verified by computational and experimental methods including advanced high-resolution solid-state NMR techniques. These results combine the advantages of fully heterogeneous systems with the tunability of molecular co-catalysts and lead the way towards true single-site COF-based photocatalytic systems with a high level of interfacial control.

## Results and discussion

In previous studies, COF-42[27] has been shown to be active in photocatalytic hydrogen evolution reactions with conventional hydrogen evolution co-catalysts such as platinum nanoparticles or molecular chloro(pyridine)cobaloxime.[14] At the same time, this COF is a well-known and versatile platform that is chemically robust due to its hydrazone-linked structure.[28,29] In this study, we used COF-42 as a platform for covalent post-synthetic modification with cobaloxime complexes. The synthesis of COF-42 by solvothermal acid-catalyzed condensation of 1,3,5-triformylbenzene (TFB) and 2,5-diethoxyterephthalohydrazide (DETH) followed published protocols.[27] In order to provide functional sites for the covalent attachment of the co-catalyst, 10 mol% of DETH was replaced by the propargyl-containing 2,5-bis(prop-2-yn-1-yloxy)terephthalohydrazide (DPTH) to obtain the propargyl-modified $pCOF_{10}$. The COFs were characterized by FT-IR spectroscopy, sorption analysis, powder X-ray diffraction (PXRD), magic-angle-spinning solid-state NMR (ssNMR), and quantum-chemical calculations.

The successful transformation of the starting materials to $pCOF_{10}$ was proven by the lack of residual aldehyde

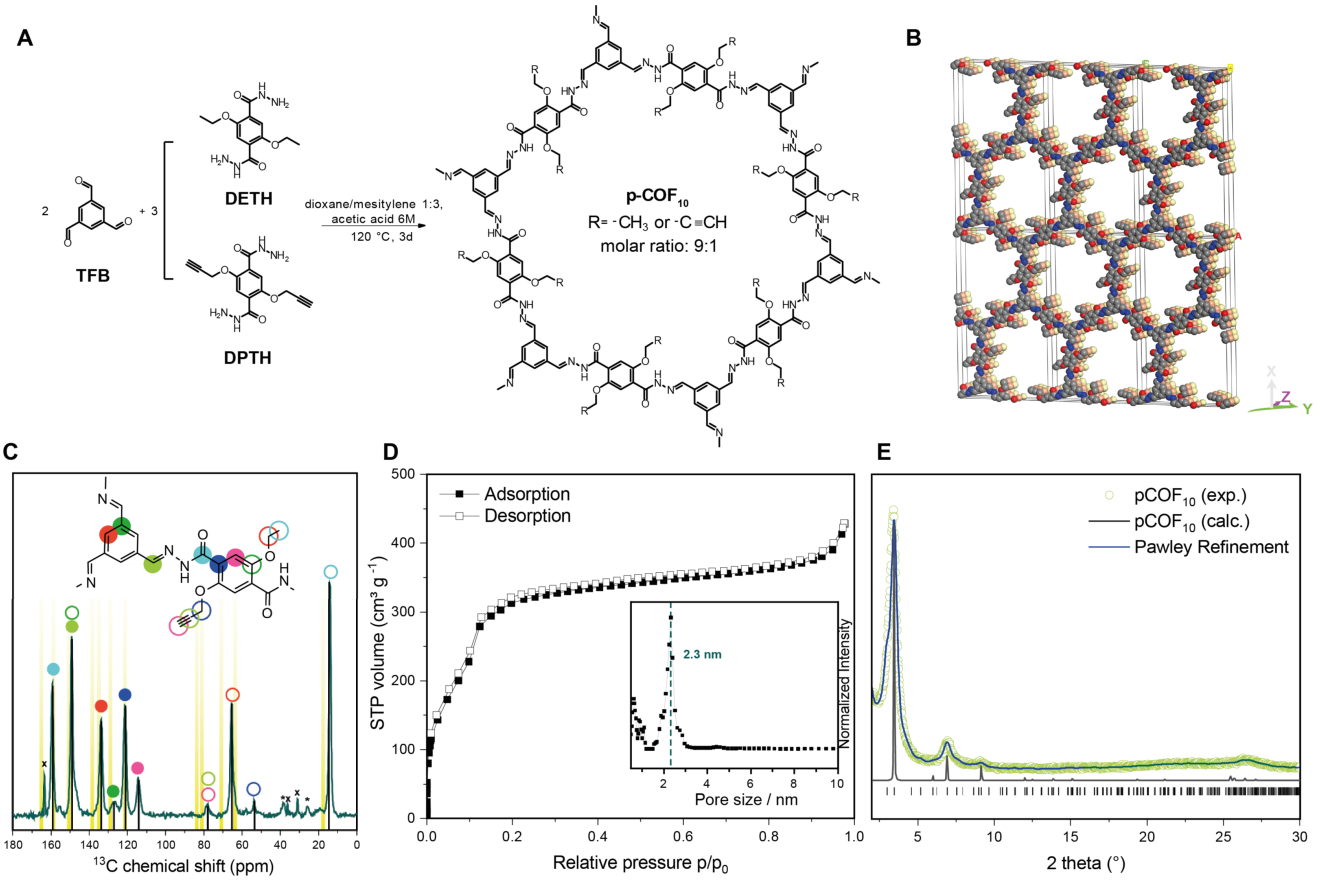


**Figure 1.** (A) Synthesis of $pCOF_{10}$ by solvothermal condensation of triformyl benzene (TFB) and a 9:1 mixture of 2,5-diethoxyterephthalohydrazide (DETH) and 2,5-bis(prop-2-yn-1-yloxy)terephthalohydrazide (DPTH). (B) Eclipsed stacking model for $pCOF_{10}$. C, N and O atoms are represented in grey, blue and red. H atoms are omitted, the second and third layer are represented in orange and yellow for clarity. (C) Solid state 1D $^{13}C\{^{1}H\}$ CP-MAS NMR spectrum of $pCOF_{10}$ acquired at 11.7 T, 12 kHz MAS, 298 K, and using cross-polarization times of 5 ms. Spinning side bands are marked with asterisks. Calculated shifts are marked with yellow bars. The narrow signals labelled with crosses at 164 ppm, 37 ppm, and 32 ppm correspond to residual dimethylformamide. (D) Argon adsorption isotherm of $pCOF_{10}$. Inlet: Pore size distribution from NLDFT calculations with cylindrical pores in equilibrium mode. Resulting main pore size is 2.3 nm. (E) PXRD pattern of $pCOF_{10}$ (open, green circles), Pawley refined profile (blue line) and calculated XRD pattern for the idealized AA stacking (black line).

stretching vibration in its FT-IR spectrum. Characteristic C=O vibrations and signals originating from the hydrazone bonds overlap at 1680 $cm^{-1}$ (see Figure S13). New vibrations emerged at 2250 $cm^{-1}$ which could be assigned to the propargyl groups confirming the successful incorporation of DPTH building blocks into the COF backbone. This was further supported by a 1D $^{13}C\{^1H\}$ ssNMR spectrum where $^{13}C$ signals at 79 and 58 ppm can be assigned to the propargyl functional group (Figure 1C). These shifts match the corresponding chemical shift of the liquid state NMR of the DPTH linker (see Supporting Information for experimental details) and are also confirmed by quantum-chemical calculations (see Table S3).

PXRD analysis confirmed the crystalline structure of $pCOF_{10}$. The PXRD pattern shows a strong reflection at 3.3° 2$\theta$ followed by smaller ones at 5.9, 7.0, 9.1 and a very broad one at 26° 2$\theta$. The experimental powder pattern was compared to a simulated one (see Figure 1E) and the diffraction peaks assigned as the 100, 101, 200, 201 and 001 reflections, respectively. The peaks are broadened due to small domain sizes in the COF particles, especially in the z direction, where the interlayer interactions are defined by $\pi$-$\pi$-stacking only. Different possible orientations for the propargyl functionality as well as slightly shifted AA' stacking modes lead to very similar powder patterns; due to broadening of the reflections in the experimental data, the different orientations can not be distinguished. One of these possible structural models is shown in Figure 1B, featuring an AA stacking mode with an interlayer distance of 3.5 Å, which is typical for structurally similar COFs.[10,30,31] Note that in the underlying structural model, one out of six DETH linkers per pore was replaced by DPTH which results in a functionalization degree of 16.6% instead of the statistically distributed 10% in the experimentally prepared $pCOF_{10}$.

Pawley refinement of the structure in the idealized AA stacking mode suggests $P2/m$ symmetry. For the modeled structure, the resulting cell parameters are $a$ = 51.09 Å, $b$ = 3.50 Å, $c$ = 29.48 Å , $\alpha = \gamma = 90.00°$ and $\beta = 89.94°$. Sorption analysis revealed a mesoporous structure with pore size of 2.3 nm and a Brunauer-Emmett-Teller (BET) surface area of 1839 $m^2\ g^{-1}$, which matches the theoretically expected values of the structural model well (see Figure 1D).

For the covalent attachment of the cobaloxime catalyst to $pCOF_{10}$, a postsynthetic click-chemistry approach was chosen. The copper(I)-catalyzed Huisgen-type cycloaddition of azines and alkynes is known to be broadly applicable with high yields and a high tolerance for functional groups.[32–36] Therefore, the pyridine which acts as axial cobaloxime ligand was functionalized with an azide group to yield the para-functionalized pyridine **1a**, which forms the azide-functionalized complex [**Co-1a**] and likewise, the meta-functionalized analogues **1b** and [**Co-1b**] were synthesized, as depicted in Figure 2. Additionally, the equatorially-functionalized chelating ligand **2** was synthesized as described in the Supporting Information. It forms the azide-functionalized catalyst [**Co-2**] by metal complexation as before. Two strategies were tested for the attachment of the cobaloxime complex to $pCOF_{10}$: *i*) metal complexation of azide-functionalized ligands with subsequent COF-modification by click-reaction with the azide-functionalized complexes, termed route I; *ii*) COF-modification by click-reaction with azide-functionalized ligands with subsequent complexation, termed route II (see Supporting Information for experimental details). The resulting COF-cobaloxime hybrid samples are labeled as follows with the respective numbering according to Figure 2: [**1a**]-COF for clicked ligands; [**Co-1a**]-COF for COF-cobaloxime hybrid samples.

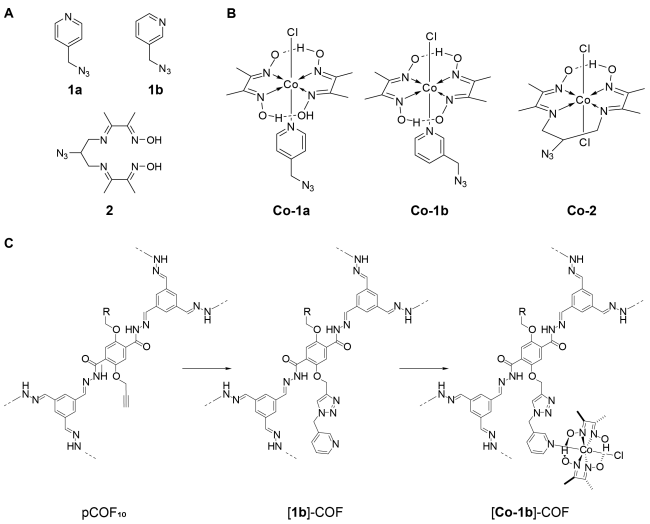


**Figure 2.** (A) Structure of the azide-functionalized ligands 1a, 1b, 2 and (B) the azide-functionalized complexes **Co-1a**, **Co-1b**, and **Co-2**. (C) Exemplary postsynthetic COF modification towards [**Co-1b**]-COF. Synthesis conditions can be found in the Supporting Information.

To verify the success of the tethering of the cobaloxime and the unperturbed structural integrity of the covalently modified hybrid COF-cobaloxime systems we performed the same systematic experimental analysis as for the intact $pCOF_{10}$. PXRD shows that the crystallinity of the COF is preserved and the stacking mode does not change with respect to $pCOF_{10}$ (Figure S6). Sorption analysis shows the expected reduction of the surface area according to Table S1. Pore size distributions for the clicked samples were calculated from Ar sorption isotherms as shown in Figure S5. In all samples, the 2.3 nm pore size, as found in $pCOF_{10}$, is preserved with lower pore volume fraction while additional smaller pores up to 1.9 nm occur as seen from optimized pore models (see Figure S19). FT-IR spectra display all expected vibrations of the COF including propargyl vibrations at ca. 3300 and 2300 $cm^{-1}$. These vibrations are still visible in ligand-tethered samples which hints to partial transformation. New triazole peaks are hidden in the region around 3100 $cm^{-1}$ due to low intensity. The success of the click reaction was further confirmed by the reduced intensity of the propargyl signals relative to the other signals in the 1D $^{13}C\{^1H\}$ CP ssNMR spectrum upon addition of the azide compounds. We did not observe any additional signals arising from the clicked compound, which is probably due to signal superposition, especially in the aromatic region, and due to lower signal intensity caused by a low functionalization degree. UV-Vis diffuse reflectance spectra show two additional broad absorption bands at 500 and 600 nm for the cobaloxime containing samples (Figure S15). These bands are due to the electronic transitions of the azide-functionalized cobaloximes. Depending on the reaction conditions (see supporting information for more details), the cobaloxime loading can be adjusted within limits. For all samples, the total cobaloxime amount was determined by ICP analysis, and for [**Co-1a**]-COF it was additionally confirmed by fast-MAS $^1H$-detected NMR spectra. The values range from 0.47 to 2.4 wt% for route II, while route I resulted in higher cobaloxime amounts between 1.2 and 8.5 wt%. The

highest cobaloxime content was found for [**Co-1a**]-COF as can be seen in Table S2. The resulting functionalization degrees ranging from 2.0 to 15% are also listed there. Scanning electron microscopy shows a flower-like morphology for all samples. Elemental mapping showed a uniform distribution of carbon, nitrogen, oxygen, and cobalt in the samples as can be seen in the Supporting Information.

### ssNMR analysis of the COF-cobaloxime hybrid systems

While powder diffraction analysis provides long-range spatial information such as approximate interlayer separations, ssNMR provides us with short-range interatomic proximities, and hints about the position of the cobaloxime inside the pore. To this end, we performed an in-depth structural analysis of the clicked samples **1a**-COF and [**Co-1a**]-COF using $^{1}$H-detected, fast-MAS ssNMR at $\nu_{\mathrm{rot}} = 55.55$ kHz at 700 MHz $^{1}$H Larmor frequency (16.4 T). The samples based on [**Co-1a**] were chosen due to higher molecular symmetry compared to [**Co-1b**]. Both **1a**-COF and [**Co-1a**]-COF were studied by 1D and 2D $^{1}$H and $^{13}$C solid-state NMR techniques. All 2D measurements were $^{1}$H-detected, which significantly improved the sensitivity of the natural abundance $^{13}$C measurements. In addition to the sensitivity gain, we could exploit the $^{1}$H chemical shifts as well as the $^{1}$H - $^{1}$H correlations as sources of structural information.

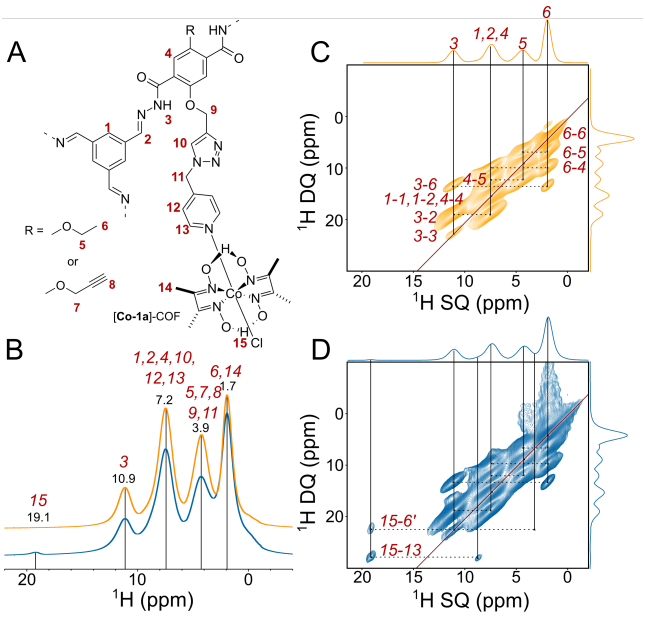


**Figure 3.** Solid-state NMR comparison of the $^{1}$H spectra of [**1a**]-COF (yellow) and [**Co-1a**]-COF (blue) measured at 700 MHz $^{1}$H Larmor frequency at $\nu_{\mathrm{rot}} = 55.55$ kHz. (A) Schematic structure of the subsection of [**Co-1a**]-COF with proton labeling. (B) 1D $^{1}$H spectra of [**1a**]-COF (yellow) and [**Co-1a**]-COF (blue). Distinct $^{1}$H resonances are given in ppm and labelled with the corresponding atom labels as displayed in (A). (C) and (D) $^{1}$H-$^{1}$H DQ-SQ correlation spectra of [**1a**]-COF (yellow) and [**Co-1a**]-COF (blue). Horizontal dashed lines indicate the $^{1}$H-$^{1}$H connectivities, and vertical solid lines reflect the individual $^{1}$H SQ resonances. Assignments are given next to the dashed lines. In (D) the assignment for only the two new connectivities are shown. The skyline projection of both dimensions are also shown.

Figure 3B compares the 1D $^{1}$H spectra of **1a**-COF (yellow) and [**Co-1a**]-COF (blue). The high structural order of these two-dimensional crystalline polymers is reflected in the good resolution of the $^{1}$H signals; $^{1}$H line widths vary between 800 and 1300 Hz for **1a**-COF and between 1000 and 2000 Hz for [**Co-1a**]-COF. In the $^{1}$H spectra, we could directly observe four (**1a**-COF) and five ([**Co-1a**]-COF) distinct proton resonances which correspond to the amide proton (10.9 ppm), aromatic protons overlapping with the olefin proton (7.2 ppm), methylene protons (3.9 ppm), and methyl protons (1.7 ppm). For [**Co-1a**]-COF, we also observe a well-separated, downfield-shifted low-intensity peak that belongs to the strongly hydrogen-bonded oxime proton (19.1 ppm). Note that all $^{1}$H signals are broader in the spectrum of [**Co-1a**]-COF relative to **1a**-COF which indicates that the cobaloxime functionalization process disrupted the overall COF crystallinity to some extent. Cobaloxime contains Co(III), which is, unlike Co(II), diamagnetic, therefore the observed line broadening of [**Co-1a**]-COF cannot be a consequence of paramagnetic relaxation enhancement; also, residual $CoCl_2$ salt is washed out during the sample preparation process. It is more likely that the post-synthetic modification reduced the crystalline domain size and increased the sample's heterogeneity leading to a wider range of chemical shifts for each sites.

The good $^{1}$H resolution of the fast-MAS $^{1}$H spectrum prompted us to measure 2D homonuclear correlation experiments to gain deeper insight into the intramolecular interaction between the COF backbone and the cobaloxime co-catalyst. We probed the relative $^{1}$H-$^{1}$H distances using a 2D double quantum-single quantum (DQ-SQ) correlation experiments employing the R-symmetry-based $R14_4^{-2}$ homonuclear recoupling sequence.[37] The $R14_4^{-2}$ is a $\gamma$-encoded symmetry sequence which suppresses all heteronuclear dipole-dipole couplings and chemical shift terms in the first-order Hamiltonian. We used a $R = \pi_0$ element as the basic R-symmetry block with a nutation frequency of 97.22 kHz ($3.5 \times \nu_{\mathrm{rot}}$). The homonuclear 2D $^{1}$H-$^{1}$H DQ-SQ recoupling experiment relies on the generation of double quantum coherences *via* homonuclear dipole-dipole coupling to obtain through-space information of nearby protons. Due to the double-quantum filter, the spectrum exhibits cross-peaks only between protons that share direct dipolar interactions with each other and thus no relayed magnetization transfer occurs. For protonated organic solid materials, such as the COFs of this study, the observation of a DQ peak is indicative of a proton-proton proximity that is $\leq 3.5$ Å.[38,39] The relative signal intensities could well approximate interatomic distances.[39]

Figure 3C and D show the $^{1}$H-$^{1}$H DQ-SQ correlation spectra of **1a**-COF (yellow) and [**Co-1a**]-COF (blue). The spectra reveal double-quantum correlations between both distinct and identical environments, appearing at the off-diagonal and diagonal positions, respectively. Diagonal peaks are expected for the signals of the methyl and methylene group, as well as between the resonances of the chemically equivalent aromatic sites. However, the weak diagonal peak for the NH protons corresponds to an NH-NH autopeak which is indicative of the dipolar interaction between COF layers; the separation of NH protons within one layer is $<$ 7 Å, while the layer-to-layer distance is 3.5 Å according to powder crystal analysis. The two spectra look almost identical, the only considerable difference being the $^{1}$H cross-peaks of the oxime $^{1}$H at 19.1 ppm with resonances at 8.7 and 3.4 ppm. In order to assign these two peaks, and thus uncover the position of cobaloxime inside the pore, we performed a detailed quantum-chemical study (*vide infra*). Based on these studies we conclude the resonances at 8.7 and 3.4 ppm to belong to the pyridine aromatic proton (H13), as well as to a downfield shifted methyl proton of a neighboring ethoxy

group with which the cobaloxime is in close contact.

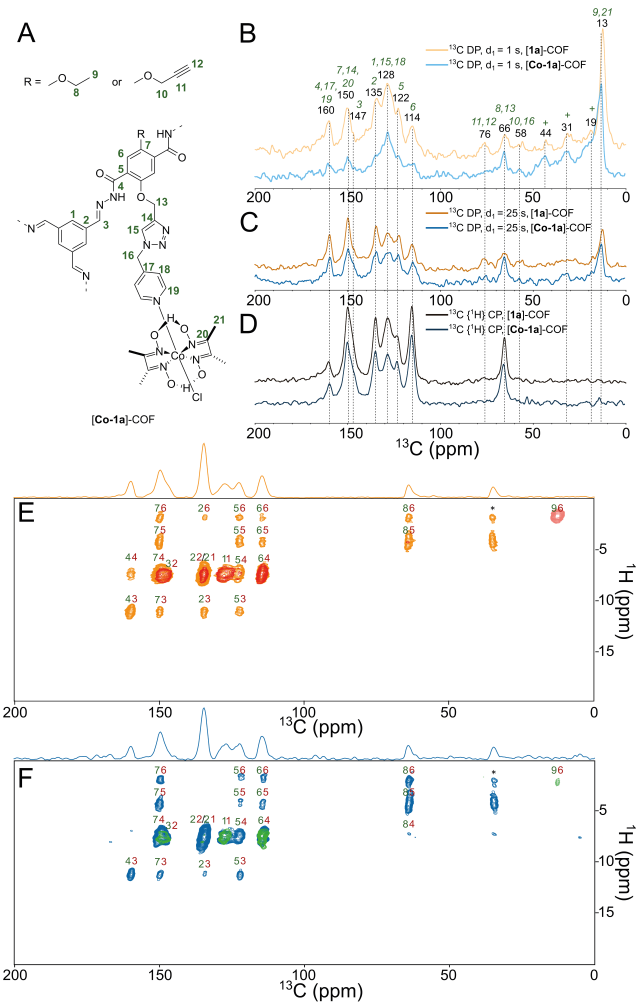


**Figure 4.** (A) Schematic structure of the subsection of [**Co-1a**]-COF with carbon labeling. (B), (C) and (D) Comparison of the natural abundance $^{13}$C one-dimensional solid-state NMR spectra of [**1a**]-COF (blue shades) and [**Co-1a**]-COF (orange shades) measured at 700 MHz $^1$H Larmor frequency at $\nu_{rot} = 55.55$ kHz. Direct polarization spectra recorded with $d_1 = 1$ s (B) or with long $d_1 = 25$ s (C) are compared with CP MAS spectra (D). For the CP MAS experiment, the carrier was centered at 130 ppm and the CP was optimized to transfer magnetization to the aromatic region. The CP contact time was 500 $\mu$s. Signals with short longitudinal relaxation times are enhanced in the $^{13}$C direct MAS spectrum measured with 1 s recycle delay. The assignment of the $^{13}$C resonances was obtained from 2D $^1$H-$^{13}$C, and $^1$H-$^1$H correlation experiments, and from the quantum chemical calculations. The signals marked with crosses correspond to impurities, e.g. to residual solvent signals.(E) and (F) $^1$H-detected 2D $^1$H-$^{13}$C correlation spectra of [**1a**]-COF (E) and [**Co-1a**]-COF (F) recorded with 500 $\mu$s (red and green), or with 2250 $\mu$s (orange and blue) CP contact times. The CP-based spectra are overlaid with INEPT-based HSQC spectra which display only one methyl cross-peak displayed with blue (E) and magenta (F) colors. For each cross peak, the $^1$H and $^{13}$C assignments are displayed with red and green colors, respectively. Signals marked with an asterisk are measurement artifacts and they do not appear in 1D $^{13}$C-detected $^{13}$C{$^1$H} CP spectra.

Next, we assessed the relative flexibility of the two compounds using 1D $^{13}$C NMR spectroscopy. Three different 1D $^{13}$C MAS spectra of [**1a**]-COF and [**Co-1a**]-COF are given in Figure 4A and B, respectively. These spectra include $^{13}$C{$^1$H} cross-polarization (CP) MAS, and $T_1$-weighted, direct-polarization (DP) $^{13}$C spectra recorded with short (1 s) and long (25 s) recycle delay times. These latter spectra were used to elucidate the relative mobility of certain sites in the COF samples. In the $^{13}$C spectra recorded with $d_1 = 1$ s those signals are more intense that have considerably shorter $^{13}$C longitudinal relaxation time constants ($T_1 < 1$ s), since the signal recovery is proportional to $1-\exp(-d_1/T_1)$. Such short $T_1$ is indicative of motions occurring on the inverse of the Larmor frequency (few nanoseconds). The longitudinal relaxation constant depends not only on the amplitude of ns time-scale motion but also on the number of directly attached protons: the more protons are directly bound to a carbon the faster it relaxes *via* heteronuclear dipolar relaxation. This is reflected in the relative change of signal intensities among the aromatic carbons. Besides, the methyl resonance relaxes rapidly due to the free rotation around the C-C axis in the ethyl group. The methyl resonance line shape in the DP spectrum of [**Co-1a**]-COF is markedly distorted presenting a shoulder at lower resonances. This signal could be assigned to the methyl carbons of the cobaloxime ligand. Otherwise, the signals of the covalently tethered ligand does not show any obvious sign of increased fast time-scale flexibility, neither for [**1a**]-COF nor for [**Co-1a**]-COF. In the spectrum of [**Co-1a**]-COF recorded with $d_1 = 1$ s the intensified resonances at 128 ppm indicate rather flexible aromatic sites, but due to strong overlaps in this region we could not identify if this signal belongs to the ligand or to some residual impurities which tend to show up stronger in $T_1$-weighted experiments. Selective $^{13}$C or $^{15}$N labeling at specified positions at the ligand would help us to quantify the amplitude and time scale of the ligand motion.

The apparent lack of high-amplitude fast time-scale dynamics of the two COF frameworks were further validated by comparing $^1$H-detected 2D CP-based $^1$H-$^{13}$C correlation spectra with INEPT-based 2D HSQC spectra (Fig. 4D, E). High-amplitude ns time-scale motion results in inherent decoupling and thus leads to increased coherent lifetimes in INEPT-based experiments and to decreased transfer efficiencies in CP-based experiments. In the HSQC spectrum of both [**1a**]-COF and [**Co-1a**]-COF we observe only a single methyl peak indicating that the COF backbone is generally rigid on the ns time scale.

## Computational studies

In order to provide a structural model for the position and the orientation of the covalently tethered cobaloxime co-catalyst inside the pore, we conducted a detailed *in silico* structural investigation of [**1a**]-COF and [**Co-1a**]-COF. Atom positions and lattices of the periodic COF structure of [1a]-COF were optimized on RI-PBE-D3/def2-TZVP [40–43] level of theory using an acceleration scheme based on the resolution of the identity (RI) technique and the continuous fast multipole method (CFMM) [44–46] implemented [47,48] in Turbomole version V7.1. [49] The obtained structure for the [**1a**]-COF was then used to prepare parameters for molecular dynamics simulations using antechamber. [50] Force field minimizations and subsequent dynamics were performed using the NAMD program package [51,52] using GAFF parameters [53] afterwards. NMR chemical shifts were then calculated on B97-2/pcSseg-1 [54,55] level of theory using the FermiONs++ [56,57] program package, using cut models of obtained structures to compare with experimental chemical shifts and assign the resonances.

Using this data, we prepared 200 *in silico* $^1$H-$^1$H DQ-SQ and $^1$H-$^{13}$C 2D correlation spectra (see Supporting Information for details) and used them to identify features that are also present in the experimentally obtained ssNMR spectra.

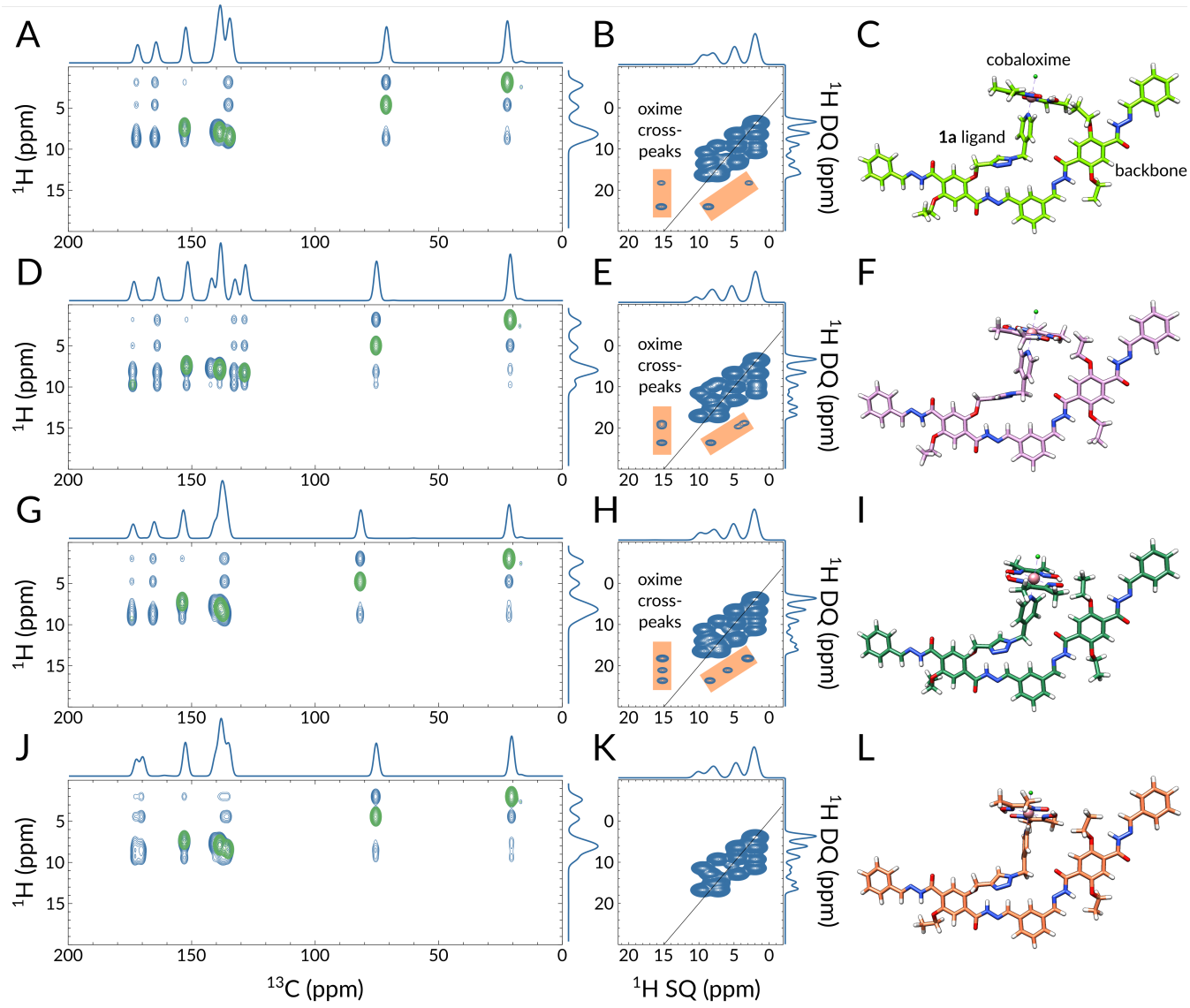


**Figure 5.** Direct comparison of quantum-chemically obtained $^1$H-$^{13}$C (A, D, G, J) and $^1$H-$^1$H DQ-SQ (B, E, H, K) 2D ssNMR spectra with corresponding structural models of [**Co-1a**]-COF on the right (C, F, I, L). For a better comparison, the same NMR chemical shift region is displayed as in the experimentally obtained spectra (Fig. 3C, D and Fig. 4D, E). In the $^1$H-$^{13}$C 2D spectra blue and green colors represent $^1$H-$^{13}$C atom pairs that are within 6 and 2 Å, respectively. In the $^1$H-$^1$H DQ-SQ spectra, the orange color highlights the oxime proton cross-peaks. In C, F, I, and L the Co, Cl, O, N, and H atoms are displayed with pink, lime, red, blue, and white colors, respectively.

Such features include the number of cross-peaks, especially cross-peaks of the oxime proton, their relative intensity ratios, and their peak positions. The most distinctive factor in the simulated $^{1}$H-$^{1}$H DQ-SQ spectra is the presence of oxime (H15) cross-peaks with resonances at around 8.7 and 3.4 ppm, which was used to categorize the simulated spectra. These distinct chemical shifts suggest that the oxime proton is interacting with an aromatic proton (at 8.7 ppm), and with either an upfield shifted methylene proton or with a downfield shifted methyl proton (at 3.4 ppm). There are four different aromatic protons in [**Co-1a**]-COF: H1, H4, H12, and H13, out of which only H4 and H13 can get closer than 3.5 Å to H15.

To decide which resonance lead to the 3.4 ppm cross-peak with H15, we analyzed the shielding effects of the glyoxime group on the nearby ethoxy methyl and methylene protons. The approach of the glyoxime oxygen towards the ethoxy group induces a deshielding effect, consequently, both the methyl and the methylene protons resonate at higher frequencies (see Fig. S16 and SI text for more details), this rules out the possibility that the cross-peak at 3.4 ppm would stem from an upfield shifted methylene proton and leaves only a downfield shifted methyl proton as a possible interaction partner. Besides, we excluded the possibility that the oxime proton shows a trivial intra-ligand cross-peak with the glyoxime methyl protons, since (*i*) the distance between the H15 and H16 protons are $>$ 3.5 Å, and (*ii*) the calculated chemical shift are below 2.9 ppm.

Out of the 200 simulated $^{1}$H-$^{1}$H DQ-SQ spectra 27 (13) contained two (three) oxime cross-peaks, among which 22 spectra have these peaks in the expected ppm range. By considering the relative peak intensity ratios between the oxime cross-peaks only 15 spectra have a more intense aromatic-oxime than a methyl-oxime cross peak. Two of such spectra, together with the simulated $^{1}$H-$^{13}$C spectra and corresponding structures, are displayed in Figure 5A-F. As counter-examples, Fig. 5G-H and J-K display the spectra of such structures (Fig. 5I and L) where three equally intense peaks (Fig. 5H) or no oxime proton cross peak (Fig. 5K) appear in the simulated DQ-SQ spectra. The possibility that in reality, in a fraction of the [**Co-1a**]-COF pores the cobaloxime does not interact with the pore wall cannot be ruled out, nonetheless, our current data suggests that when it does, it gets in close contact with the nearby ethoxy group. It is also likely that this genuine interaction stabilizes the complex and restricts the cocatalyst's degradation during the photocatalytic cycles. Note that at this stage, both the ssNMR measurements and the *in silico* calculations were performed in a solvent-free environment. Future ssNMR measurements with added acetonitrile/water mixture accompanied with simulations in explicit solvent could reveal if the cobaloxime stays attached to the pore wall or wether it gains more flexibility and drifts towards the pore center.

To inspect the spacial arrangement inside the pore, we modelled [**Co-1a**]-COF including one tethered co-catalyst based on the MD simulated structures (Fig. 6). The displayed ligand has the same orientation as in Fig. 5C. From the side and front views it is apparent that the ligand spreads over multiple layers and occupies a substantial portion of the pore. Due to spacial confinements our model suggest that no more than three [**Co-1a**] over three layers can fit into the backbone, i.e. the maximum number of [**Co-1a**] per layer is one. In our case, we have 13 mol% functionalization which translates into one [**Co-1a**] for every seven layers.

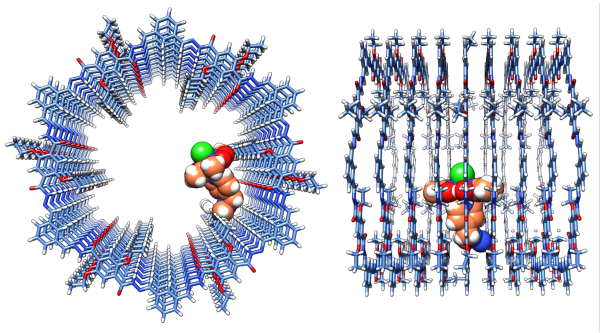

**Figure 6.** Front and side views of the MD simulated structural model of [**Co-1a**]-COF showing a possible arrangement of the co-catalyst. The linker and the cobaloxime group is depicted by spheres and their carbon atoms are displayed with orange color. Co, Cl, O, N, and H atoms are displayed with pink, lime, red, blue, and white colors, C atoms of the backbone is light blue.

### Photocatalytic activity

To probe whether there is a possible benefit of covalent co-catalyst immobilization over simple physisorption,[14,15] the COF-cobaloxime hybrid samples were tested for photocatalytic activity. In a typical photocatalysis experiment, 5 mg of COF hybrid were suspended in 10 mL of acetonitrile and water in a ratio of 4:1 at pH 8 containing 100 µL triethanolamine (TEOA) as sacrificial donor. A housed Xe lamp was used to illuminate the suspension interface with a nominal beam spectral distribution similar to AM1.5G. The beam intensity before experiments was then adjusted to 100 mW cm$^{-2}$. See ESI for more details. Photocatalytic Hydrogen Evolution Reaction (HER) rates were quantified in a continuous flow reactor as previously reported[15] (Figure 7A). As a reference system, we compared the hybrid systems to samples where [**Co-1a**] or [**Co-1b**] were added to the suspension and physisorbed to COF-42 with a BET surface area of 2336 m$^{2}$ g$^{-1}$ during photocatalysis. The maximum photonic efficiencies after *in situ* photoactivation of the samples ranging from 2 to 8 wt% cobaloxime catalyst according to ICP results can be found in Figure 7A. In the physisorbed samples, an increase of the photonic efficiency was found when increasing the catalyst amount from 2 to 4 wt% with a maximum efficiency of 0.06% for [**Co-1a**] and 0.07% for [**Co-1b**] at 4.0 wt%, while the efficiency is fairly constant at higher percentages (0.06% to 0.08% at 5.0 and 8.0 wt%) for [**Co-1b**]. This behaviour is expected for the system as in the low-loading region, the photocatalytic activity scales linearly with the co-catalyst amount while it reaches a maximum in the higher-loading region where the availability of the co-catalyst is not limiting anymore.

In the hybrid samples, an activity maximum rather than a constant behavior is found for each hybrid type. For the para-functionalized [**Co-1a**], the highest photonic efficiency was found at 4.1 wt%, while for the meta-functionalized [**Co-1b**] the maximum was found at 3.2 wt%. As before, a linear increase of the photonic efficiency in the low-loading regime was observed. However, further increase in cobaloxime loading resulted in lower activity in the immobilized samples. We attribute this to a predominant pore clogging effect of the active sites with increasing functionalization. In general, the highest photonic efficiency was achieved with [**Co-1a**]-COF with 0.14% followed by [**Co-1b**]-COF with 0.11% Compared to the physisorbed samples with the corresponding cobaloxime content, the activ-

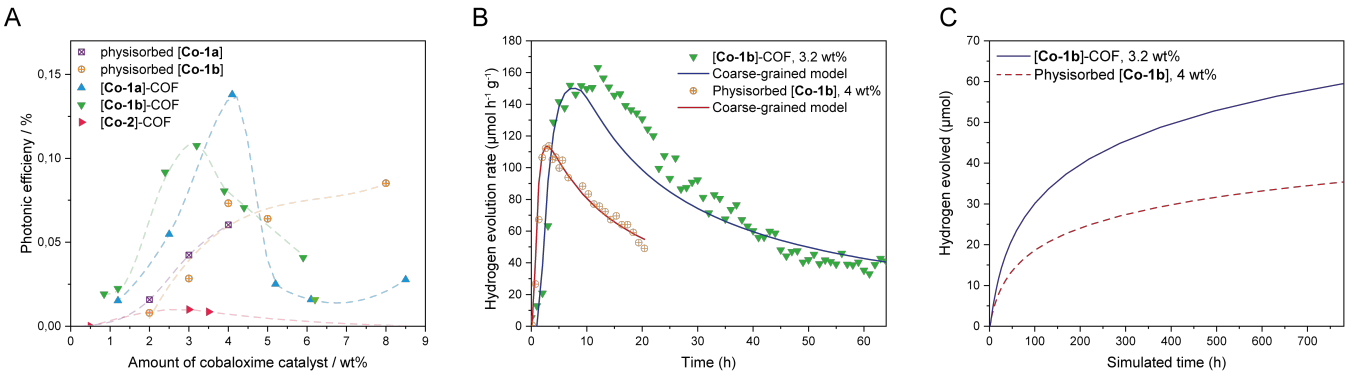


**Figure 7.** (A) Comparison of photonic efficiencies for hybrid samples and COF-42 with physisorbed [**Co-1a**] and [**Co-1b**]. (B) Comparison of the hydrogen evolution rate of [**Co-1b**]-COF containing 3.2 wt% [**Co-1b**] and COF-42 with 4.0 wt% physisorbed [**Co-1b**] and coarse-grained model fits of both systems. (C) Projection of the hydrogen evolution of [**Co-1b**]-COF containing 3.2 wt% [**Co-1b**] and COF-42 with 4.0 wt% physisorbed [**Co-1b**] based on the coarse-grained models.

ity doubles for both systems. Additionally, to emphasize the role of the complex environment of the cobaloxime over the pure presence of Co(II) we performed a measurement where we added $CoCl_2$ to a suspension of $pCOF_{10}$ and triethanolamine in the photocatalysis medium as well as experiments where one of the components (COF, TEOA) was excluded (see Supporting Information). None of the reference samples showed hydrogen evolution after several hours of irradiation. For the hybrid samples, the close contact between the cobaloxime and the COF pore wall—revealed by representative solid state NMR and computational studies (*vide supra*) with [**Co-1a**]-COF—might facilitate charge transfer to the cobaloxime catalyst from the COF pore wall as also observed from photoluminescence measurements (see Figure S11 and Figure S12) [**Co-2**]-COF shows a significantly lower activity in $CH_3CN/H_2O$ which is a known effect for cobaloximes that lack equatorial protons. The protonation of the oxime oxygen, which is necessary for the catalytic process, is hindered in those cases.[58,59] The catalytic activity could not be improved by lowering the pH to 4. In this case, different acids (ascorbic acid, acetic acid, and citric acid) were tested which simultaneously served as sacrificial electron donors instead of the amine base TEOA. Even though the stability of [**Co-2**]-COF is predicted to be higher than for the other tested cobaloximes, the complex proved not to be appropriate in our case. We compared the best performing [**Co-1b**]-COF sample (containing 3.2 wt% cobaloxime) to COF-42 physisorbed with [**Co-1b**]. A sample with the same amount of physisorbed cobaloxime was qualitatively active in photocatalytic hydrogen evolution, but for precise quantification we increased the catalyst amount to 4.0 wt%. Even though it contained 20% less catalyst, the hybrid sample was 47% more active than the physisorbed one (163 vs. 111 µmol $h^{-1}$ $g^{-1}$), see Figure 7A. Additionally, the long-term stability increased significantly. After 20 h, the physisorbed sample shows 52% of its initial activity, while the hybrid sample maintains 80% of its initial activity. To get an estimate of the longevity of the systems, we fitted the hydrogen evolution rates of both samples with a coarse-grained model (Figure 7C) that was established in an earlier study on photocatalysis with COFs and a Nickel-based oligomer as co-catalyst.[15] The model resulted in very precise fitting for the physisorbed catalyst because of similarities to the original Nickel-based system from where the coarse-grain fitting model was obtained, while the hybrid sample showed a more complex behaviour that is not perfectly mapped with this simplified model. Based on the coarse-grained fits, we projected the total amount of hydrogen evolved by the samples at full depletion (see Figure 7C). After 780 h, the projection of the physisorbed sample reaches 35 µmol hydrogen evolved while the value is 59 µmol for the hybrid sample, which is a gain of 69%. Comparing the estimated turnover number (TON) of both systems, the deviation gets even more obvious. While the TON after 780 h is simulated to be 81 for the physisorbed sample, it increases by 110% to a value of 170 in the hybrid sample. We attribute this activity enhancement to the local confinement in the COF-hybrid samples as supported by MD simulations.

Cobaloximes are known to slowly decompose under photocatalytic conditions. The labile axial pyridine ligand decoordinates in the catalytic cycle due to a square-planar Co(II) transition state. The catalyst in solution can then possibly be reduced which limits its stability. Due to the confinement between ligand and catalyst in the COF pores, the re-coordination might be enhanced, hence counteracting degradation, which leads to reactivation of the catalyst. Additionally, charge transfer is favoured in the case of spatial proximity of the co-catalyst and the pore wall. Both effects result in higher overall activity as well as longevity. Interestingly, the activation period for the hybrid samples is significantly longer than for the physisorbed ones. This may be attributed to the time-delayed accessibility of the catalyst in the pores. Both limitations could be addressed *via* a method that was recently published by Thomas et al.,[60,61] where silica spheres were used to create an inverse-opal architecture in the COF material. The so created macropores could serve as channels for reagents and products. Also, immobilization of the co-catalyst in a COF with larger pores might have a similar effect.

## Conclusion

In summary, we have developed a platform derived from COF-42 as a support for the immobilization of cobaloxime catalysts. The post-synthetic modification of propargyl-functionalized COF-42 enabled the covalent tethering of three different cobaloximes to form COF-cobaloxime hybrid systems. This tethering significantly enhanced the photocatalytic activity of the system by more than 100% compared to the physisorbates with the corresponding cobaloxime amount. The high crystallinity of our materials allowed for an in-depth solid-state 2D NMR characterization using fast MAS and proton detection. In the 1D $^1H$ spectrum of

[**Co-1a**]-COF we could clearly identify the resonance corresponding to the oxime proton based on its highly downfield shifted resonance. The 2D $^{1}$H-$^{1}$H Dq-Sq experiment showed two cross-peaks for the oxime proton consistent with the incorporation of the co-catalyst into the COF material. MD simulations with subsequent quantum-chemical NMR chemical shift calculations allowed us to locate the position of the tethered ligand inside the pore based on the experimentally observed oxime proton cross peaks. Our analysis suggests that the cobaloxime in [**Co-1a**]-COF closely interacts with the pore wall. We surmise this interaction is responsible both for the improved photocatalytic activity and for the prolonged activity of the hybrid samples with respect to the physisorbed variant. We anticipate that larger pore channels or the addition of dedicated transport pores will further improve the pore accessibility and prevent back-reaction *via* local confinement of the products, thereby further increasing increase the hydrogen evolution activity of the system even further.

## Associated Content

### Supporting Information

Experimental procedures, COF synthesis, details of molecular dynamic simulations and quantum chemical calculations and additional measurements.

## Author Information

### Corresponding Authors

Bettina V. Lotsch (b.lotsch@fkf.mpg.de)

### Notes

The authors declare no competing financial interests.

**Acknowledgement** Financial support is gratefully acknowledged from the Max Planck Society, an ERC Starting Grant (project COF Leaf, grant number 639233), the Deutsche Forschungsgemeinschaft (DFG) via the SFB 1333 (project A03), the Cluster of Excellence e-conversion, and the Center for Nanoscience. PR acknowledges the Deutsche Forschungsgemeinschaft (DFG, German Research Foundation) SFB 1309 – 325871075, project A3 and Fonds der Chemischen Industrie. We thank Prof. T. Bein and Prof. W. Schnick (University of Munich, LMU) for granting access to the XRD facility and V. Duppel and M.-L. Schreiber for the assistance with material analysis.

## References

(1) Li, L.; Cai, Z.; Wu, Q.; Lo, W.-Y.; Zhang, N.; Chen, L. X.; Yu, L. Rational Design of Porous Conjugated Polymers and Roles of Residual Palladium for Photocatalytic Hydrogen Production. *J. Am. Chem. Soc.* **2016**, *138*, 7681–7686.

(2) Zhang, Y.; Mao, F.; Wang, L.; Yuan, H.; Liu, P. F.; Yang, H. G. Recent Advances in Photocatalysis over Metal–Organic Frameworks-Based Materials. *Solar RRL* **2019**, 1900438.

(3) Diercks, C. S.; Liu, Y.; Cordova, K. E.; Yaghi, O. M. The role of reticular chemistry in the design of CO2 reduction catalysts. *Nat. Mater.* **2018**, *17*, 301–307.

(4) Vyas, V. S.; hei Lau, V. W.; Lotsch, B. V. Soft Photocatalysis: Organic Polymers for Solar Fuel Production. *Chem. Mater.* **2016**, *28*, 5191–5204.

(5) Sick, T.; Hufnagel, A. G.; Kampmann, J.; Kondofersky, I.; Calik, M.; Rotter, J. M.; Evans, A.; Döblinger, M.; Herbert, S.; Peters, K.; Böhm, D.; Knochel, P.; Medina, D. D.; Fattakhova-Rohlfing, D.; Bein, T. Oriented Films of Conjugated 2D Covalent Organic Frameworks as Photocathodes for Water Splitting. *J. Am. Chem. Soc.* **2017**, *140*, 2085–2092.

(6) Côté, A. P.; Benin, A. I.; Ockwig, N. W.; O&039,; Keeffe, M.; Matzger, A. J.; Yaghi, O. M. Porous, Crystalline, Covalent Organic Frameworks. *Science* **2005**, *310*, 1166.

(7) Tilford, R. W.; Mugavero, S. J.; Pellechia, P. J.; Lavigne, J. J. Tailoring Microporosity in Covalent Organic Frameworks. *Adv. Mater.* **2008**, *20*, 2741–2746.

(8) Ding, S.-Y.; Wang, W. Covalent organic frameworks (COFs): from design to applications. *Chem. Soc. Rev.* **2013**, *42*, 548–568.

(9) Lohse, M. S.; Bein, T. Covalent Organic Frameworks: Structures, Synthesis, and Applications. *Adv. Funct. Mater.* **2018**, *28*, 1705553.

(10) Stegbauer, L.; Schwinghammer, K.; Lotsch, B. V. A hydrazone-based covalent organic framework for photocatalytic hydrogen production. *Chem. Sci.* **2014**, *5*, 2789–2793.

(11) Haase, F.; Banerjee, T.; Savasci, G.; Ochsenfeld, C.; Lotsch, B. V. Structure–property–activity relationships in a pyridine containing azine-linked covalent organic framework for photocatalytic hydrogen evolution. *Faraday Discuss.* **2017**, *201*, 247–264.

(12) Stegbauer, L.; Zech, S.; Savasci, G.; Banerjee, T.; Podjaski, F.; Schwinghammer, K.; Ochsenfeld, C.; Lotsch, B. V. Tailor-Made Photoconductive Pyrene-Based Covalent Organic Frameworks for Visible-Light Driven Hydrogen Generation. *Adv. Energy Mater.* **2018**, *8*, 1703278.

(13) Wang, X.; Chen, L.; Chong, S. Y.; Little, M. A.; Wu, Y.; Zhu, W.-H.; Clowes, R.; Yan, Y.; Zwijnenburg, M. A.; Sprick, R. S.; Cooper, A. I. Sulfone-containing covalent organic frameworks for photocatalytic hydrogen evolution from water. *Nat. Chem.* **2018**, *10*, 1180–1189.

(14) Banerjee, T.; Haase, F.; Savasci, G.; Gottschling, K.; Ochsenfeld, C.; Lotsch, B. V. Single-Site Photocatalytic H2 Evolution from Covalent Organic Frameworks with Molecular Cobaloxime Co-Catalysts. *J. Am. Chem. Soc.* **2017**, *139*, 16228–16234.

(15) Biswal, B. P.; Vignolo-González, H. A.; Banerjee, T.; Grunenberg, L.; Savasci, G.; Gottschling, K.; Nuss, J.; Ochsenfeld, C.; Lotsch, B. V. Sustained Solar H2 Evolution from a Thiazolo[5,4-d]thiazole-Bridged Covalent Organic Framework and Nickel-Thiolate Cluster in Water. *J. Am. Chem. Soc.* **2019**, *141*, 11082–11092.

(16) Banerjee, T.; Gottschling, K.; Savasci, G.; Ochsenfeld, C.; Lotsch, B. V. H2 Evolution with Covalent Organic Framework Photocatalysts. *ACS Energy Letters* **2018**, *3*, 400–409.

(17) Dempsey, J. L.; Brunschwig, B. S.; Winkler, J. R.; Gray, H. B. Hydrogen Evolution Catalyzed by Cobaloximes. *Acc. Chem. Res.* **2009**, *42*, 1995–2004.

(18) Artero, V.; Chavarot-Kerlidou, M.; Fontecave, M. Splitting Water with Cobalt. *Angew. Chem. Int. Ed.* **2011**, *50*, 7238–7266.

(19) Muresan, N. M.; Willkomm, J.; Mersch, D.; Vaynzof, Y.; Reisner, E. Immobilization of a Molecular Cobaloxime Catalyst for Hydrogen Evolution on a Mesoporous Metal Oxide Electrode. *Angew. Chem. Int. Ed.* **2012**, *51*, 12749–12753.

(20) Nasalevich, M. A.; Becker, R.; Ramos-Fernandez, E. V.; Castellanos, S.; Veber, S. L.; Fedin, M. V.; Kapteijn, F.; Reek, J. N. H.; van der Vlugt, J. I.; Gascon, J. Co@NH2-MIL-125(Ti): cobaloxime-derived metal–organic framework-based composite for light-driven H2 production. *Energy & Environmental Science* **2015**, *8*, 364–375.

(21) Gao, L.-F.; Zhu, Z.-Y.; Feng, W.-S.; Wang, Q.; Zhang, H.-L. Disentangling the Photocatalytic Hydrogen Evolution Mechanism of One Homogeneous Cobalt-Coordinated Polymer. *The Journal of Physical Chemistry C* **2016**, *120*, 28456–28462.

(22) Cao, S.-W.; Liu, X.-F.; Yuan, Y.-P.; Zhang, Z.-Y.; Fang, J.; Loo, S. C. J.; Barber, J.; Sum, T. C.; Xue, C. Artificial photosynthetic hydrogen evolution over g-C3N4 nanosheets coupled with cobaloxime. *Phys. Chem. Chem. Phys.* **2013**, *15*, 18363.

(23) Li, X.; Masters, A. F.; Maschmeyer, T. Photocatalytic Hydrogen Evolution from Silica-Templated Polymeric Graphitic Carbon Nitride-Is the Surface Area Important? *ChemCatChem* **2014**, *7*, 121–126.

(24) Lazarides, T.; McCormick, T.; Du, P.; Luo, G.; Lindley, B.; Eisenberg, R. Making Hydrogen from Water Using a Homogeneous System Without Noble Metals. *J. Am. Chem. Soc.* **2009**, *131*, 9192–9194.

(25) Lakadamyali, F.; Reisner, E. Photocatalytic H2 evolution from neutral water with a molecular cobalt catalyst on a dye-sensitised TiO2 nanoparticle. *Chem. Commun.* **2011**, *47*, 1695.

(26) Yin, M.; Ma, S.; Wu, C.; Fan, Y. A noble-metal-free photocatalytic hydrogen production system based on cobalt(iii) complex and eosin Y-sensitized TiO2. *RSC Advances* **2015**, *5*, 1852–1858.

(27) Uribe-Romo, F. J.; Doonan, C. J.; Furukawa, H.; Oisaki, K.; Yaghi, O. M. Crystalline Covalent Organic Frameworks with Hydrazone Linkages. *J. Am. Chem. Soc.* **2011**, *133*, 11478–11481.

(28) Gottschling, K.; Stegbauer, L.; Savasci, G.; Prisco, N. A.; Berkson, Z. J.; Ochsenfeld, C.; Chmelka, B. F.; Lotsch, B. V. Molecular Insights into Carbon Dioxide Sorption in Hydrazone-Based Covalent Organic Frameworks with Tertiary Amine Moieties. *Chem. Mater.* **2019**, *31*, 1946–1955.

(29) Zhang, Y.; Shen, X.; Feng, X.; Xia, H.; Mu, Y.; Liu, X. Covalent organic frameworks as pH responsive signaling scaffolds. *Chem. Commun.* **2016**, *52*, 11088–11091.

(30) Chen, X.; Addicoat, M.; Jin, E.; Xu, H.; Hayashi, T.; Xu, F.; Huang, N.; Irle, S.; Jiang, D. Designed synthesis of double-stage two-dimensional covalent organic frameworks. *Sci. Rep.* **2015**, *5*, 14650.

(31) Li, Z.-J.; Ding, S.-Y.; Xue, H.-D.; Cao, W.; Wang, W. Synthesis of –C=N– linked covalent organic frameworks via the direct condensation of acetals and amines. *Chem. Commun.* **2016**, *52*, 7217–7220.

(32) Himo, F.; Lovell, T.; Hilgraf, R.; Rostovtsev, V. V.; Noodleman, L.; Sharpless, K. B.; Fokin, V. V. Copper(I)-Catalyzed Synthesis of Azoles. DFT Study Predicts Unprecedented Reactivity and Intermediates. *J. Am. Chem. Soc.* **2005**, *127*, 210–216.

(33) Rostovtsev, V. V.; Green, L. G.; Fokin, V. V.; Sharpless, K. B. A Stepwise Huisgen Cycloaddition Process: Copper(I)-Catalyzed Regioselective "Ligation" of Azides and Terminal Alkynes. *Angew. Chem. Int. Ed.* **2002**, *41*, 2596–2599.

(34) Hein, C. D.; Liu, X.-M.; Wang, D. Click Chemistry, A Powerful Tool for Pharmaceutical Sciences. *Pharm. Res.* **2008**, *25*, 2216–2230.

(35) Amblard, F.; Cho, J. H.; Schinazi, R. F. Cu(I)-Catalyzed Huisgen Azide-Alkyne 1,3-Dipolar Cycloaddition Reaction in Nucleoside, Nucleotide, and Oligonucleotide Chemistry. *Chem. Rev.* **2009**, *109*, 4207–4220.

(36) Meldal, M.; Tornøe, C. W. Cu-Catalyzed Azide-Alkyne Cycloaddition. *Chem. Rev.* **2008**, *108*, 2952–3015.

(37) Levitt, M. H. *Symmetry-Based Pulse Sequences in Magic-Angle Spinning Solid-State NMR*; American Cancer Society, 2007; pp 1–31.

(38) Brown, S. P.; Lesage, A.; Elena, B.; Emsley, L. Probing Proton-Proton Proximities in the Solid State: High-Resolution Two-Dimensional1H-1H Double-Quantum CRAMPS NMR Spectroscopy. *J. Am. Chem. Soc.* **2004**, *126*, 13230–13231.

(39) Bradley, J. P.; Tripon, C.; Filip, C.; Brown, S. P. Determining relative proton–proton proximities from the build-up of two-dimensional correlation peaks in 1H double-quantum MAS NMR: insight from multi-spin density-matrix simulations. *Phys. Chem. Chem. Phys.* **2009**, *11*, 6941.

(40) Perdew, J. P.; Burke, K.; Ernzerhof, M. Generalized Gradient Approximation Made Simple. *Phys. Rev. Lett.* **1996**, *77*, 3865–3868.

(41) Grimme, S.; Antony, J.; Ehrlich, S.; Krieg, H. A consistent and accurate ab initio parametrization of density functional dispersion correction (DFT-D) for the 94 elements H-Pu. *The Journal of Chemical Physics* **2010**, *132*, 154104.

(42) Schäfer, A.; Huber, C.; Ahlrichs, R. Fully optimized contracted Gaussian basis sets of triple zeta valence quality for atoms Li to Kr. *The Journal of Chemical Physics* **1994**, *100*, 5829–5835.

(43) Eichkorn, K.; Weigend, F.; Treutler, O.; Ahlrichs, R. Auxiliary basis sets for main row atoms and transition metals and their use to approximate Coulomb potentials. *Theoretical Chemistry Accounts: Theory, Computation, and Modeling (Theoretica Chimica Acta)* **1997**, *97*, 119–124.

(44) Burow, A. M.; Sierka, M.; Mohamed, F. Resolution of identity approximation for the Coulomb term in molecular and periodic systems. *The Journal of Chemical Physics* **2009**, *131*, 214101.

(45) Grajciar, L. Low-memory iterative density fitting. *J. Comput. Chem.* **2015**, *36*, 1521–1535.

(46) Burow, A. M.; Sierka, M. Linear Scaling Hierarchical Integration Scheme for the Exchange-Correlation Term in Molecular and Periodic Systems. *J. Chem. Theory Comput.* **2011**, *7*, 3097–3104.

(47) Łazarski, R.; Burow, A. M.; Sierka, M. Density Functional Theory for Molecular and Periodic Systems Using Density Fitting and Continuous Fast Multipole Methods. *J. Chem. Theory Comput.* **2015**, *11*, 3029–3041.

(48) Łazarski, R.; Burow, A. M.; Grajciar, L.; Sierka, M. Density functional theory for molecular and periodic systems using density fitting and continuous fast multipole method: Analytical gradients. *J. Comput. Chem.* **2016**, *37*, 2518–2526.

(49) TURBOMOLE (V7.1 2016). University of Karlsruhe and Forschungszentrum Karlsruhe GmbH, 1989-2007, TURBOMOLE GmbH, since 2007. Available at http://www.turbomole.com.

(50) Wang, J.; Wang, W.; Kollman, P. A.; Case, D. A. Automatic atom type and bond type perception in molecular mechanical calculations. *J. Mol. Graphics Modell.* **2006**, *25*, 247–260.

(51) Phillips, J. C.; Braun, R.; Wang, W.; Gumbart, J.; Tajkhorshid, E.; Villa, E.; Chipot, C.; Skeel, R. D.; Kalé, L.; Schulten, K. Scalable molecular dynamics with NAMD. *J. Comput. Chem.* **2005**, *26*, 1781–1802.

(52) Case, D. A.; Betz, R. M.; Cerutti, D. S.; Cheatham, III, T. E.; Darden, T. A.; Duke, R. E.; Giese, T. J.; Gohlke, H.; Goetz, A. W.; Homeyer, N.; Izadi, S.; Janowski, P.; Kaus, J.; Kovalenko, A.; Lee, T. S.; LeGrand, S.; Li. P.; Lin, C.; Luchko, T.; Lu, R.; Madej, B.; Mermelstein, D.; Merz, K. M.; Monard, G.; Nguyen, H.; Nguyen, H. T.; Omelyan, I.; Onufriev, A.; Roe, D. R.; Roitberg, A.; Sagui, C.; Simmerling, C. L.; Botello-Smith, W. M.; Swails, J.; Walker, R. C.; Wang, J.; Wolf, R. M.; Wu, X.; Xiao, L.; Kollman, P. A. (2016), AMBER 2016, University of California, San Francisco.

(53) Wang, J.; Wolf, R. M.; Caldwell, J. W.; Kollman, P. A.; Case, D. A. Development and testing of a general amber force field. *J. Comput. Chem.* **2004**, *25*, 1157–1174.

(54) Wilson, P. J.; Bradley, T. J.; Tozer, D. J. Hybrid exchange-correlation functional determined from thermochemical data and ab initio potentials. *The Journal of Chemical Physics* **2001**, *115*, 9233–9242.

(55) Jensen, F. Segmented Contracted Basis Sets Optimized for Nuclear Magnetic Shielding. *J. Chem. Theory Comput.* **2014**, *11*, 132–138.

(56) Kussmann, J.; Ochsenfeld, C. Preselective Screening for Linear-Scaling Exact Exchange-Gradient Calculations for Graphics Processing Units and General Strong-Scaling Massively Parallel Calculations. *J. Chem. Theory Comput.* **2015**, *11*, 918–922.

(57) Kussmann, J.; Ochsenfeld, C. Pre-selective screening for matrix elements in linear-scaling exact exchange calculations. *The Journal of Chemical Physics* **2013**, *138*, 134114.

(58) Bhattacharjee, A.; Andreiadis, E. S.; Chavarot-Kerlidou, M.; Fontecave, M.; Field, M. J.; Artero, V. A Computational Study of the Mechanism of Hydrogen Evolution by Cobalt(Diimine-Dioxime) Catalysts. *Chemistry - A European Journal* **2013**, *19*, 15166–15174.

(59) Kaeffer, N.; Chavarot-Kerlidou, M.; Artero, V. Hydrogen Evolution Catalyzed by Cobalt Diimine–Dioxime Complexes. *Acc. Chem. Res.* **2015**, *48*, 1286–1295.

(60) Zhao, X.; Pachfule, P.; Li, S.; Langenhahn, T.; Ye, M.; Schlesiger, C.; Praetz, S.; Schmidt, J.; Thomas, A. Macro/Microporous Covalent Organic Frameworks for Efficient Electrocatalysis. *J. Am. Chem. Soc.* **2019**, *141*, 6623–6630.

(61) Zhao, X.; Pachfule, P.; Li, S.; Langenhahn, T.; Ye, M.; Tian, G.; Schmidt, J.; Thomas, A. Silica-Templated Covalent Organic Framework-Derived Fe–N-Doped Mesoporous Carbon as Oxygen Reduction Electrocatalyst. *Chem. Mater.* **2019**, *31*, 3274–3280.

# Graphical TOC Entry